



Technical Note

Investigating Wintertime Cloud Microphysical Properties and Their Relationship to Air Mass Advection at Ny-Ålesund, Svalbard Using the Synergy of a Cloud Radar–Ceilometer–Microwave Radiometer

Yeonsoo Cho ¹, Sang-Jong Park ² , Joo-Hong Kim ², Huidong Yeo ¹, Jihyun Nam ¹, Sang-Yoon Jun ², Baek-Min Kim ³ and Sang-Woo Kim ^{1,*} 

¹ School of Earth and Environmental Sciences, Seoul National University, Seoul 08826, Korea; whdustn21@snu.ac.kr (Y.C.); hdyeo@snu.ac.kr (H.Y.); jihnam@snu.ac.kr (J.N.)

² Korea Polar Research Institute, Incheon 21990, Korea; sangjong@kopri.re.kr (S.-J.P.); joo-hong.kim@kopri.re.kr (J.-H.K.); syjun@kopri.re.kr (S.-Y.J.)

³ Department of Environmental Atmospheric Sciences, Pukyong National University, Busan 48513, Korea; baekmin@pknu.ac.kr

* Correspondence: sangwookim@snu.ac.kr



Citation: Cho, Y.; Park, S.-J.; Kim, J.-H.; Yeo, H.; Nam, J.; Jun, S.-Y.; Kim, B.-M.; Kim, S.-W. Investigating Wintertime Cloud Microphysical Properties and Their Relationship to Air Mass Advection at Ny-Ålesund, Svalbard Using the Synergy of a Cloud Radar–Ceilometer–Microwave Radiometer. *Remote Sens.* **2021**, *13*, 2529. <https://doi.org/10.3390/rs13132529>

Academic Editors: Maria João Costa and Michaël Sicard

Received: 24 May 2021

Accepted: 24 June 2021

Published: 28 June 2021

Abstract: This study investigates the relationship of cloud properties and radiative effects with air mass origin during the winter (November–February, 2016–2020) at Ny-Ålesund, Svalbard, through a combination of cloud radar, ceilometer, and microwave radiometer measurements. The liquid cloud fraction (CF) was less than 2%, whereas the ice CF predominantly exceeded 10% below 6 km. The liquid water content (LWC) of mixed-phase clouds (LWC_{mix}), which predominantly exist in the boundary layer (CF_{mix} : 10–30%), was approximately four times higher than that of liquid clouds (LWC_{liq}). Warm air mass advection ($warm_{adv}$) cases were closely linked with strong southerly/southwesterly winds, whereas northerly winds brought cold and dry air masses ($cold_{adv}$) to the study area. Elevated values of LWC and ice water content (IWC) during $warm_{adv}$ cases can be explained by the presence of mixed-phase clouds in the boundary layer and ice clouds in the middle troposphere. Consistently, the r_e of ice particles in $warm_{adv}$ cases was approximately 5–10 μm larger than that in $cold_{adv}$ cases at all altitudes. A high CF and cloud water content in $warm_{adv}$ cases contributed to a 33% ($69 W m^{-2}$) increase in downward longwave (LW) fluxes compared to cloud-free conditions.

Keywords: Arctic clouds; cloud microphysical properties; air mass advection; cloud radar; Ny-Ålesund

Publisher's Note: MDPI stays neutral with regard to jurisdictional claims in published maps and institutional affiliations.



Copyright: © 2021 by the authors. Licensee MDPI, Basel, Switzerland. This article is an open access article distributed under the terms and conditions of the Creative Commons Attribution (CC BY) license (<https://creativecommons.org/licenses/by/4.0/>).

1. Introduction

Cloud-related radiative processes have a major impact on the Arctic surface energy budget and Arctic warming feedbacks [1–3]. During the boreal winter (December–February), net cloud radiative forcing at the Arctic surface is approximately 10s of $W m^{-2}$, despite almost zero incoming solar radiation; this is due to the strong longwave radiative effect of Arctic clouds [4–6]. Therefore, the near-surface temperature in the Arctic during the winter is considerably affected by clouds, particularly cloud macrophysical (e.g., frequency of occurrence and vertical distribution) and microphysical (e.g., cloud phase, liquid/ice water content, and hydrometeor size distribution) properties [7,8].

Furthermore, recent rapid regional warming on the Atlantic side of the Arctic (Svalbard, Greenland Sea, Barents Sea, and Kara Sea) is greatly affected by the increased intrusion of warm and moist air masses from the North Atlantic Ocean, particularly in the wintertime, under Arctic warming triggered by greenhouse-induced global warming [9–14]. Many observational studies have also noted that cloud cover and cloud microphysical

properties over the Atlantic Arctic region are strongly influenced by large-scale atmospheric circulation [15–18]. Specifically, low-level optically thick clouds, particularly mixed-phase clouds (i.e., a mixture of liquid droplets and ice particles), are ubiquitous during winter and persist for up to several days under a variety of meteorological conditions [3,19,20]. To better understand the processes governing cloud–radiation interactions related to unprecedented warming on the Atlantic side of the Arctic, observation-based analysis is required to determine the impact of air mass origin under regional-scale atmospheric circulation on changes in cloud properties.

Ny-Ålesund, located on the west coastline of Svalbard between the Greenland Sea and the Barents Sea, is a unique station for monitoring cloud properties and cloud-related processes in the Atlantic Arctic region. Continuous vertically resolved observations of the atmosphere and clouds by various ground-based remote sensing instruments at Ny-Ålesund have previously been used to analyze cloud properties, including highly complex cloud radiative processes and their effect on near-surface temperature [15,16,21,22].

The objective of this study is to investigate the relationship between air mass advection and cloud properties and associated longwave radiative effects at Ny-Ålesund, Svalbard, during the winter months (from November to February). Data of cloud fraction, height, and microphysical parameters derived from combined ground-based radar–lidar–radiometer measurements are analyzed to demonstrate that the origin of air masses has a clear impact not only on the observed cloud properties (e.g., cloud occurrence, liquid water content, ice water content, and effective radius) but also on cloud longwave radiative effects.

2. Measurements and Analysis

Continuous cloud radar measurements, conducted as part of the Cloudnet [23], have been performed at AWIPEV research base in Ny-Ålesund (78.92° N, 11.92° E), Svalbard, since June 2016 (expect, October 2018–June 2019) within the “Arctic Amplification: Climate Relevant Atmospheric and Surface Processes, and Feedback Mechanisms (AC)³” project [24]. Collocated ceilometer and microwave radiometer (MWR) measurements were made by the Alfred Wegener Institute for Polar and Marine Research (AWI). This coordinated set of ground-based remote sensing instruments enables the determination of vertically resolved microphysical cloud properties as well as cloud boundary heights under various meteorological conditions.

In this study, we used the reflectivity factor (Z), Doppler velocity, and Doppler spectral width at vertical and temporal resolutions of 4–17 m and 2.5 s, respectively, obtained from a zenith-pointing 94-GHz cloud radar of the University of Cologne (model: JOYRAD-94), which is a Frequency-Modulated, Continuous-Wave (FMCW) Doppler W-band radar, to identify the presence of in-cloud particles, such as rain, drizzle drops, and ice particles [25]. This radar was also used to detect cloud top altitudes. The ceilometer (model: Vaisala CL51) detects attenuated backscatter coefficients (β) at 905 nm from atmospheric targets such as cloud droplets or aerosol particles at vertical and temporal resolutions of 10 m and 12–20 s, respectively [26]. It is capable of detecting the cloud base altitude, as well as the cloud top height up to a certain penetration depth depending on the optical thickness of the cloud layer (i.e., due to signal attenuation within the cloud layer) [27]. Cloud top and base height information were estimated from these two active sensors [8,19,28]. Both cloud radar and ceilometer data were downloaded from the Cloudnet (<https://cloudnet.fmi.fi/>; accessed on 26 June 2021). The MWR is an RPG-HATPRO water vapor and oxygen multichannel microwave profiler [29,30], which measures brightness temperatures in the K-band (22.24–31.40 GHz) and V-band (51.26–58.00 GHz). This instrument allows us to retrieve the liquid water path (LWP), integrated water vapor (IWV), and temperature profiles [31]. MWR profiles have a decreasing vertical resolution with altitude and a temporal resolution of approximately 1–2 s. All MWR data were downloaded from PANGAEA (<https://doi.pangaea.de/10.1594/PANGAEA.902183>; accessed on 26 June 2021) [32].

Through the combined use of these three measurements, we identified the cloud layers (i.e., cloud base and top heights), then determined the cloud phases of each cloud layer

(i.e., cloud type) as either liquid, ice, or mixed-phase clouds. Cloud heights and sub-type classification retrieved every 30 s and 20 m by the methods of Illingworth et al. [23] and Hogan and O'Connor [33] were analyzed. More details of the cloud layer and phase identification methods adopted in this study are given in Nomokonova et al. [34] and Gierens et al. [17]. All profiles for precipitating clouds were excluded in this study (approximately 3% of total observations) because the signal-to-noise ratio was not large enough to meet the data quality criteria [34].

The microphysical properties of clouds (i.e., liquid water content (LWC), ice water content (IWC), and effective radius (r_e)) provided in Cloudnet and PANGAEA (<https://doi.pangaea.de/10.1594/PANGAEA.898556>; accessed on 26 June 2021) [35] were derived by applying the empirical equations summarized in Table 1 [21,34]. By combining the MWR-derived LWP with the modeled temperature (T) and pressure (P), which were taken from GDAS1 and a numerical weather prediction (NWP) ICON model used in the Cloudnet algorithm, LWC was obtained according to the scaled adiabatic method. The IWC and ice water path (IWP) were retrieved using the empirical formula with radar-measured Z and T values from Hogan et al. [36]. The r_e of liquid droplets was calculated by the method given in Frisch et al. [37], assuming a cloud droplet concentration of 74 cm^{-3} [38]. Similarly, the r_e of ice particles was calculated using the equation proposed by Delanoë et al. [39] with the IWC and extinction coefficient (α) [36]. According to Hogan et al. [36] and Nomokonova et al. [34], the uncertainties of retrieved IWC in Cloudnet are known to be -50% – $+100\%$ and -33% – $+50\%$ at a temperature below -40°C and above -20°C , respectively. Uncertainties for retrieved r_e are about 30% for liquid droplets and about 20% for ice particles [21].

Table 1. Retrieval methods of cloud microphysical properties.

Parameter	Equation	Reference
Liquid water content (LWC)	Scaled adiabatic method using LWP from MWR	Illingworth et al. [23]
Ice water content (IWC)	$\log_{10}(\text{IWC}) = (0.00058) ZT + (0.0923) Z - (0.00706) T - 0.992$ $Z = 0.7194 \times Z_{\text{measured}}$	Hogan et al. [36]
Effective radius (liquid)	$r_e(h) = \frac{Z^{\frac{1}{6}}(h)}{2LWP^{\frac{1}{3}}} \left(\frac{\pi\rho}{6} \right)^{\frac{1}{3}} \left(\sum_{i=1}^{i=m} Z^{\frac{1}{2}}(h_i) \Delta h \right)^{\frac{1}{3}} \exp(-2\sigma_x^2)$	Frisch et al. [37]
Effective radius (ice)	$r_e = \frac{3(\text{IWC})}{2\rho_i\alpha} 10^6$ $\log_{10}(\alpha) = (0.000876) ZT + (0.0928) Z - (0.00513) T - 2.49$	Delanoë et al. [39]

Z = Radar reflectivity factor. T = Temperature. h_i = Height in the cloud (i: radar range gate at cloud base and top). Δh = Radar range gate thickness. ρ = Water density. ρ_i = Solid ice density ($0.917 \times 10^6 \text{ g cm}^{-3}$). σ_x = Logarithmic spread of the distribution (assume 0.38) [38]. α = Visible extinction coefficient.

3. Results and Discussion

3.1. Wintertime Cloud Microphysical Properties at Ny-Ålesund, Svalbard

Figure 1 shows the monthly variations of cloud fraction (CF; i.e., frequency of cloud occurrence), and cloud microphysical properties (i.e., LWC, IWC, and r_e) for liquid, ice, and mixed-phase clouds from November to February at Ny-Ålesund. The liquid cloud fraction (CF_{liq}) was less than 2% during winter months because monthly mean temperatures were below the freezing point (0°C) at all altitudes (Figure 1a). Conversely, the fraction of ice clouds (CF_{ice}) typically exceeded 10% below 6 km, corresponding to temperatures between -50°C and -10°C (Figure 1a). A distinctly high CF_{ice} near the surface in January and February may be attributed to ice precipitation in the clear sky, which is referred to as diamond dust and frequently observed in winter over other Arctic stations [40, 41]. Similar to previous studies that revealed the presence of mixed-phase clouds in the lower Arctic troposphere from radar–lidar synergetic measurements [3,19,20], we also observed ubiquitous mixed-phase clouds during winter, with estimated CF_{mix} values

of 10–30% below 2 km altitude (Figure 1a), where air temperatures of -15°C to 0°C are favorable for the coexistence of ice and liquid [41,42]. This result is consistent with Nomokonova et al. [34] and Gierens et al. [17]; there were very few liquid clouds, but mixed-phase and ice clouds were common during winter.

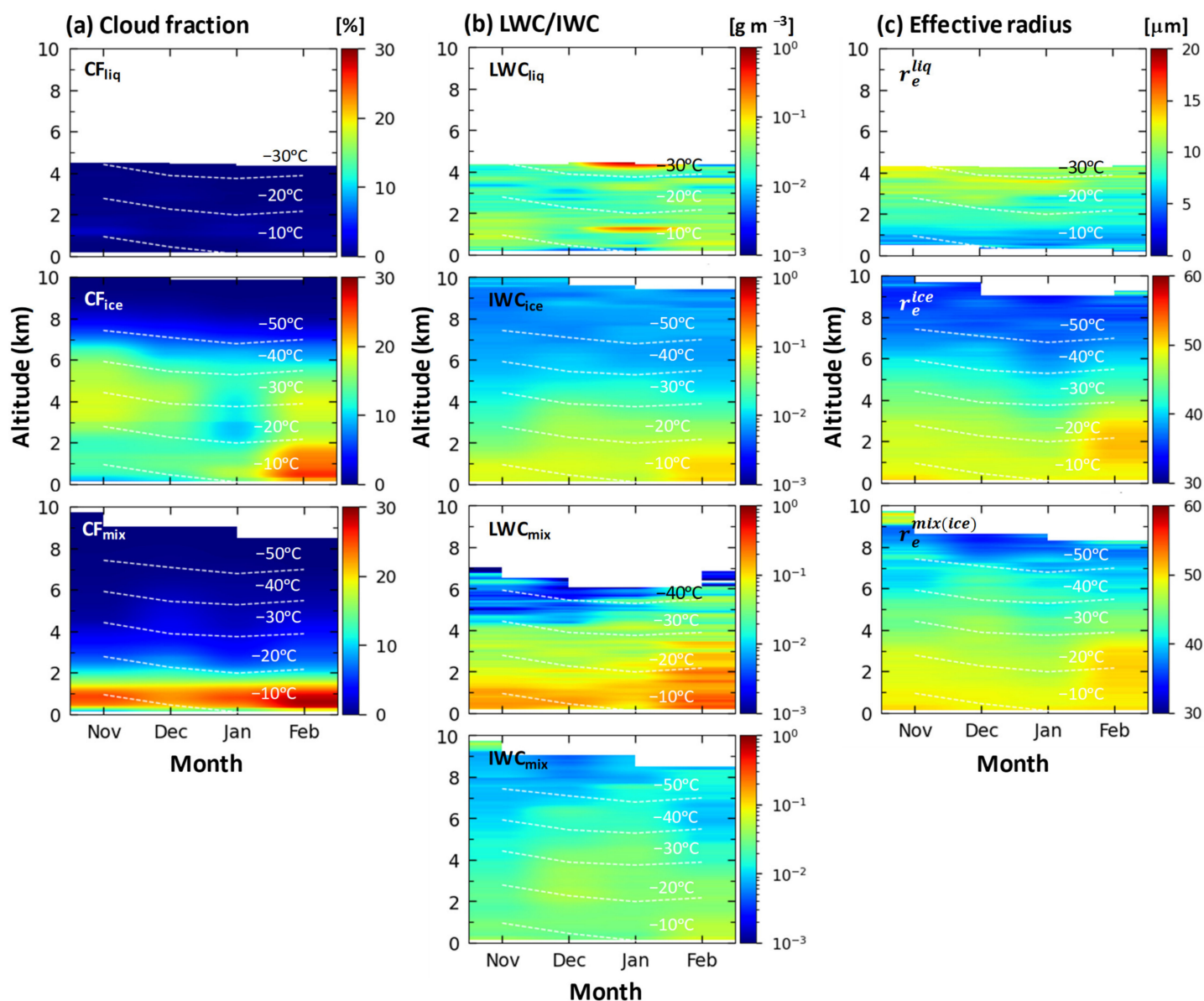


Figure 1. Monthly mean vertical distributions of (a) cloud fraction (CF), (b) liquid and ice water content (LWC/IWC), and (c) effective radius (r_e) for liquid, ice, and mixed-phase clouds during winter months (November–February) at Ny-Ålesund. White horizontal dashed line indicates the model-derived isotherm with intervals of 10°C . Note that the ranges of r_e between liquid droplets ($0\text{--}20\text{ }\mu\text{m}$) and ice particles ($30\text{--}60\text{ }\mu\text{m}$) in (c) are different.

The LWC of mixed-phase clouds (LWC_{mix}), which decreased with increasing altitude, was approximately four times higher than the LWC of liquid clouds (LWC_{liq} ; Figure 1b). LWC_{liq} was approximately constant with altitude ($0.02\text{--}0.04\text{ g m}^{-3}$). The IWC of ice clouds (IWC_{ice}) and mixed-phase clouds (IWC_{mix}) decreased with increasing altitude (Figure 1b). IWC_{mix} was about half of IWC_{ice} below 2.5 km altitude but slightly higher (~ 1.3 times) above 2.5 km . Meanwhile, phase partitioning between LWC_{mix} and IWC_{mix} plays an important role in determining the cloud radiative effects due to the strong interaction of liquid water with

radiation [7,43]. In this study, LWC_{mix} was more than twice as high as IWC_{mix} below 2 km altitude (Figure 1b) [44].

The r_e value of liquid clouds (r_e^{liq}) generally increased with altitude, and its mean value was $8.79 \pm 2.1 \mu m$ (Figure 1c). In contrast, both the r_e of ice clouds (r_e^{ice}) and ice particles in mixed-phase clouds ($r_e^{mix(ice)}$) decreased with increasing altitude, indicating that ice particles may grow as they fall [45]. The $r_e^{mix(ice)}$ value ($44.4 \pm 4.4 \mu m$) was slightly higher than the r_e^{ice} value ($42.5 \pm 5.1 \mu m$) at a 99% statistical confidence level. This can be explained by the Wegener–Bergeron–Findeisen (WBF) mechanism, in which ice particles grow rapidly in mixed-phase conditions [46–48]. As discussed later in Section 3.2, not only the peaks of IWC_{ice} , IWC_{mix} , and LWC_{mix} , but also the presence of large ice particles ($>50 \mu m$) below 3 km in February are attributed to warm and moist air masses advected from the North Atlantic Ocean to the study region. Abundant water vapor may facilitate the new formation or growth of liquid droplets, ice particles, or even snow precipitation, as reported by many studies [49,50].

These microphysical cloud properties at Ny-Ålesund are comparable with those observed at two other Cloudnet stations over the Atlantic Arctic: Andøya ($69.14^\circ N$, $15.68^\circ E$, 0.013 km above mean sea level) in northern Norway and Summit ($72.6^\circ N$, $38.4^\circ W$, 3.216 km above mean sea level) in Greenland. The winter-mean CF_{all} over Ny-Ålesund peaked by 43% at an altitude of 0.5–1.5 km due to the high CF of ice and mixed-phase clouds (Figure 2a). The CF_{ice} at Ny-Ålesund was almost constant ($\sim 18\%$) from the surface to approximately 6 km altitude.

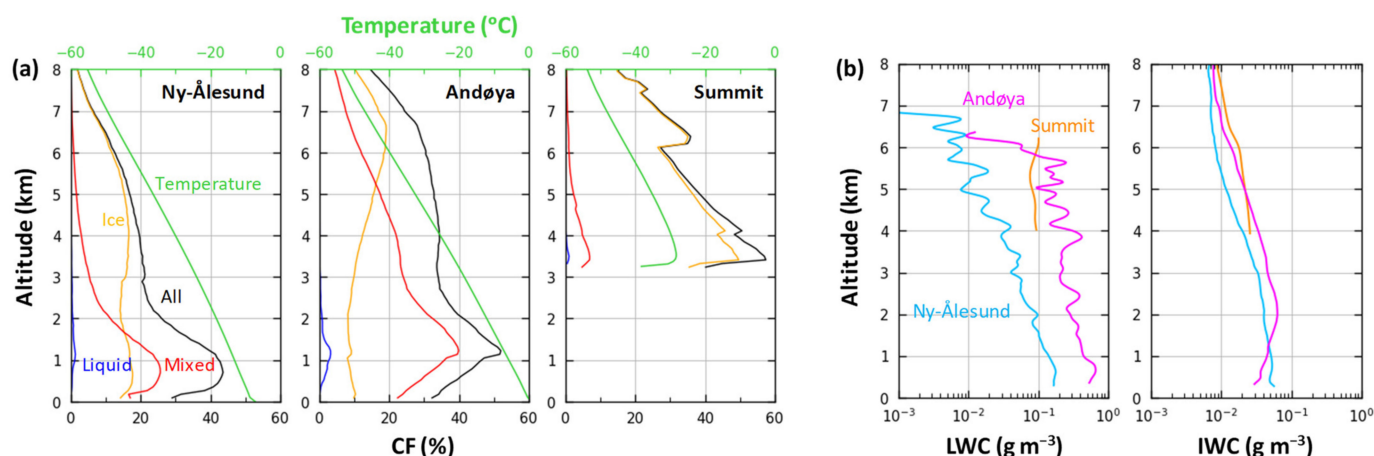


Figure 2. Vertical profiles of the wintertime mean (a) CF and (b) LWC/IWC at three sites (Ny-Ålesund, Andøya, and Summit) on the Atlantic side of the Arctic. In (a), colored line denotes CF of all (black), liquid (blue), ice (yellow), and mixed-phase (red) clouds, respectively, and green line indicates air temperature. In (b), LWC and IWC are indicated by sky-blue- (Ny-Ålesund), magenta- (Andøya), and orange- (Summit) colored lines.

The CF_{ice} below 5 km altitude at Andøya was slightly lower than that at Ny-Ålesund, but the CF_{all} was approximately 10–20% higher at Andøya due to the high CF_{mix} at all altitudes. This is because the Andøya station, which is located approximately 10° south of Ny-Ålesund, is more frequently influenced by warm and moist air masses from the Norwegian Sea during winter [51,52]. As shown in Figure 2a, the winter-mean temperature at Andøya was approximately $8^\circ C$ higher than that in Ny-Ålesund. In such a situation, where both liquid droplets and ice particles commonly coexist in the low-level cloud layer [3,53,54], the cloud phase was classified as mixed-phase clouds at both Ny-Ålesund and Andøya sites, which resulted in a relatively low CF_{liq} . The CF_{ice} at Summit was overwhelmingly higher ($\sim 20\%$) than that at the other two stations due to low atmospheric temperature. In this context, the LWC at Ny-Ålesund was approximately three (eight) times lower in the lower (middle) troposphere than that at Andøya, although the vertical

structure of LWCs was similar (Figure 2b). Unlike the LWC, the difference in IWCs among the three stations was relatively small ($\sim 0.01\text{--}0.02\text{ g}\cdot\text{m}^{-3}$; Figure 2b). As discussed in Section 3.2, the occurrence of lower tropospheric mixed-phase clouds at Ny-Ålesund and Andøya during wintertime can be associated with the advection of warm and moist air masses from the North Atlantic Ocean.

3.2. Cloud Microphysical Properties According to Warm and Cold Air Mass Advection

Air mass pathways and meteorological characteristics with different patterns are assumed to directly influence cloud formation and its microphysical properties over the study area.

Figure 3 shows the time–height plot of air temperature and a time series of LWP and IWP at Ny-Ålesund during the winter months. As explained by several previous studies, variability of near-surface temperature and cloud cover over the Atlantic Arctic region is related to regional-scale atmospheric circulation [15,16]; however, we also found distinct changes not only in modeled air temperatures in the lower and middle troposphere but also in both LWP and IWP due to shifts from cold to warm air masses on a multi-day time scale. In this study, a total of 18 warm air mass advection (hereafter, $warm_{adv}$) and 12 cold air mass advection (hereafter, $cold_{adv}$) cases were determined by the lower and upper fifth percentile periods of mean temperature bias from the surface and 1.5 km, respectively, which were calculated by subtracting each monthly mean temperature from the hourly mean temperature.

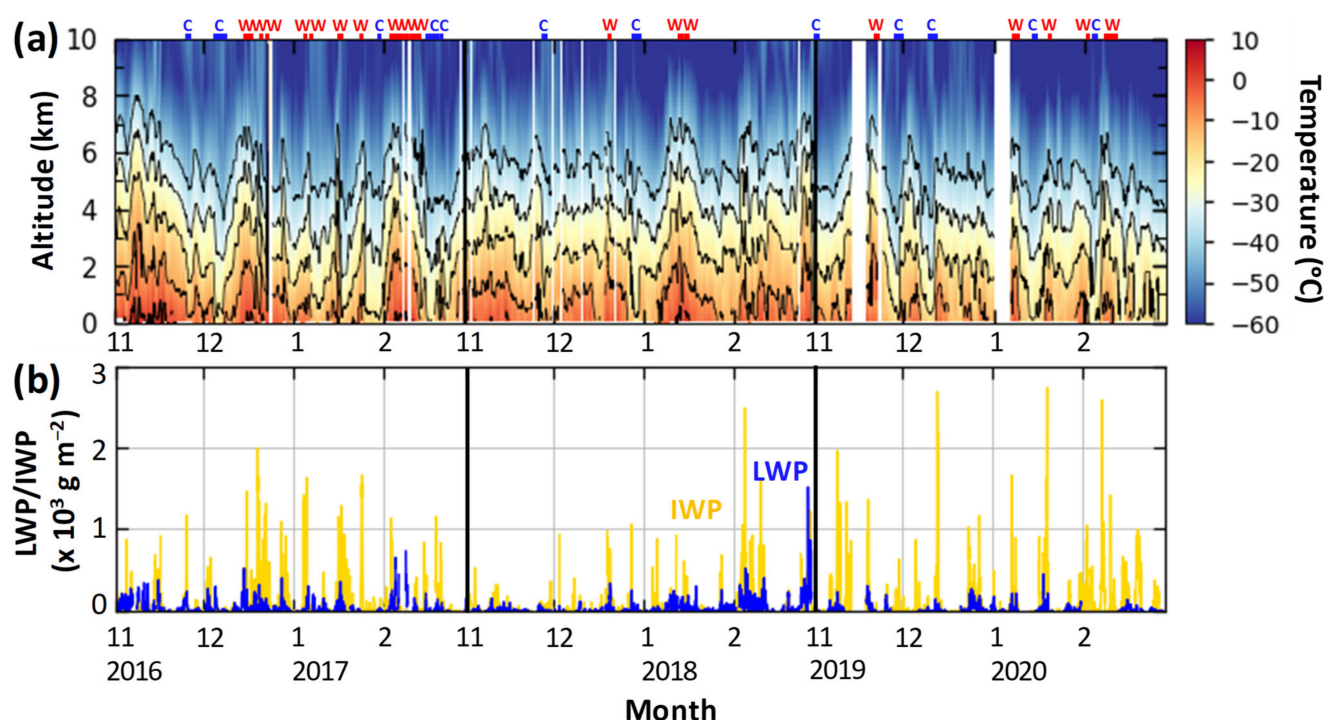


Figure 3. (a) Time–height plot of air temperatures and (b) a time series of LWP (blue)/IWP (yellow) during multi-year winter (November–February). Red and blue boxes labeled “W” and “C” on top of (a) indicate warm and cold air mass periods, respectively.

Figure 4 contrasts the regional-scale atmospheric circulation patterns over the Atlantic Arctic between $warm_{adv}$ and $cold_{adv}$ cases. Here, the 850-hPa horizontal wind and the geopotential height from ERA5 reanalysis data (<https://www.ecmwf.int/en/forecasts/datasets/reanalysis-datasets/era5>; accessed on 26 June 2021) were composited for each advection case. The $warm_{adv}$ periods were closely linked with strong southerly/southwesterly winds developed between the Icelandic Low over the south of Greenland (denoted as “L”

in Figure 4a) and the high-pressure system over northern Europe (including the Scandinavian Peninsula; denoted as “H” in Figure 4a), which can bring enormous warm and moist air masses from the North Atlantic Ocean into Ny-Ålesund (Figure 4a) [11,16,55]. Abrupt warm and humid conditions in the study area were also triggered by the appearance of a strong Atlantic windstorm [12,14]. Conversely, northerly winds developed by the low-pressure system centered over the Barents Sea and the Kara Sea (denoted as “L”) brought cold and dry air masses to the study area from the central Arctic (Figure 4b).

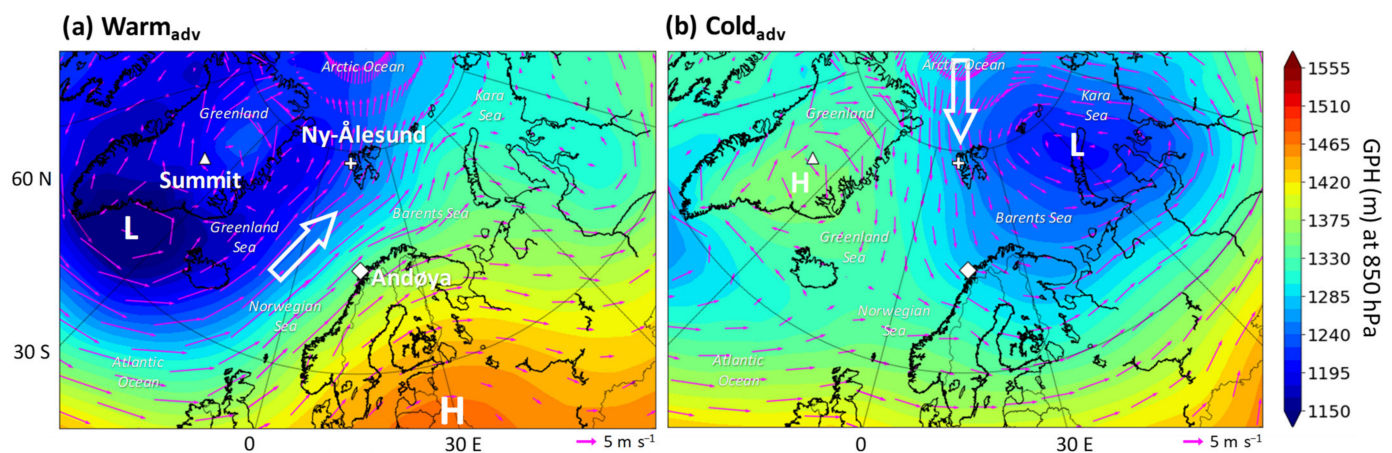


Figure 4. Mean geopotential height (GPH) and wind fields at 850 hPa pressure level (ERA5 reanalysis data) for (a) $warm_{adv}$ and (b) $cold_{adv}$ cases. Locations of Ny-Ålesund, Andøya, and Summit are denoted with “crosshair,” “diamond,” and “triangle” symbols, respectively. White arrow represents the dominant wind direction around Ny-Ålesund during two periods. “L” and “H” denote the low-pressure system (cyclone) and high-pressure system (anticyclone), respectively.

In this context, a high occurrence of clouds, especially both mixed-phase and ice clouds, and associated large LWC/IWC values was observed in $warm_{adv}$ cases (Figures 5 and 6). The total CF of $warm_{adv}$ cases showed a peak around 0.5 km (~60%) due to a high CF_{mix} (~30%) and was approximately 20–40% above 2 km altitude (Figure 5a). As mentioned earlier, the CF_{ice} during $warm_{adv}$ periods was notably high in the middle troposphere (~23%) compared to $cold_{adv}$ periods. The CF_{mix} decreased monotonically with increasing altitude. The total CF and the occurrence of mixed-phase clouds in the lower troposphere during $cold_{adv}$ cases were approximately half to one-third of those during $warm_{adv}$ cases (Figure 5b). Ice clouds (CF_{ice} : ~10%) were predominantly observed above 3 km altitude in $cold_{adv}$ cases.

Compared to $cold_{adv}$ cases, elevated values of LWC and IWC during $warm_{adv}$ cases (Figure 6a,b) can be explained by the presence of mixed-phase clouds in the boundary layer and ice clouds in the middle troposphere. This can be attributable to moisture transported from the North Atlantic Ocean [56], as illustrated in Figure 4. Nomokonova et al. [22] also reported that moist anomalies (+IWV) at Ny-Ålesund led to an increase of LWP and IWP by 1.5–2 times and 3 times, respectively, relative to normal conditions in winter. Consistently, the r_e of ice particles in $warm_{adv}$ cases was approximately 5–10 μm larger than that of $cold_{adv}$ cases at all altitudes (Figure 6c). Ice particles under warm and moist air masses can grow rapidly through aggregation or riming [45,57,58].

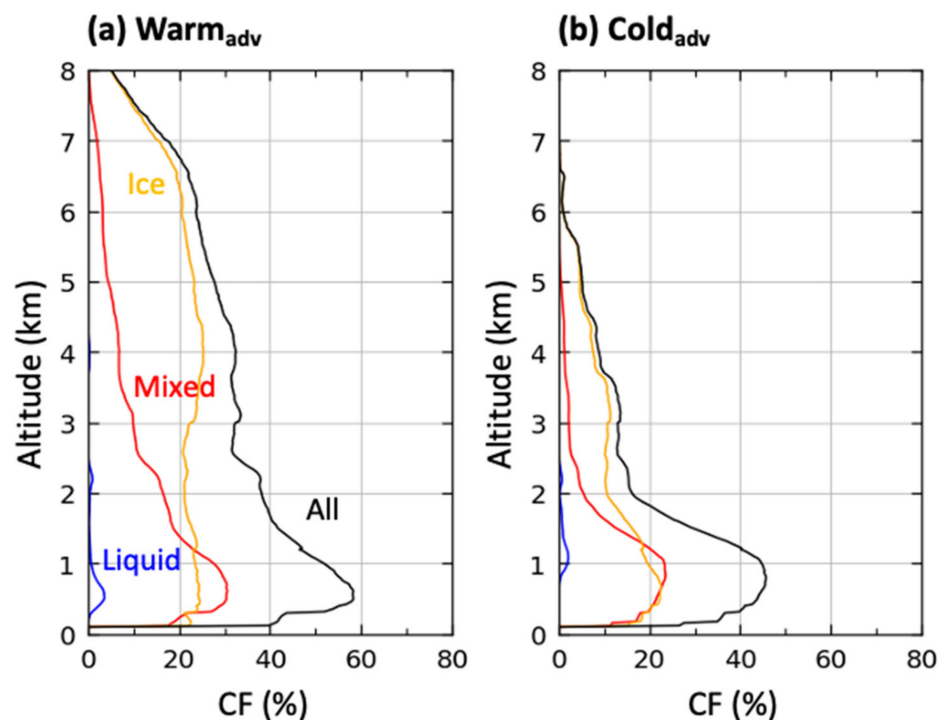


Figure 5. Vertical distributions of CF for different cloud phases (all: black, liquid: blue, ice: yellow, mixed-phase clouds: red) during (a) $warm_{adv}$ and (b) $cold_{adv}$ cases.

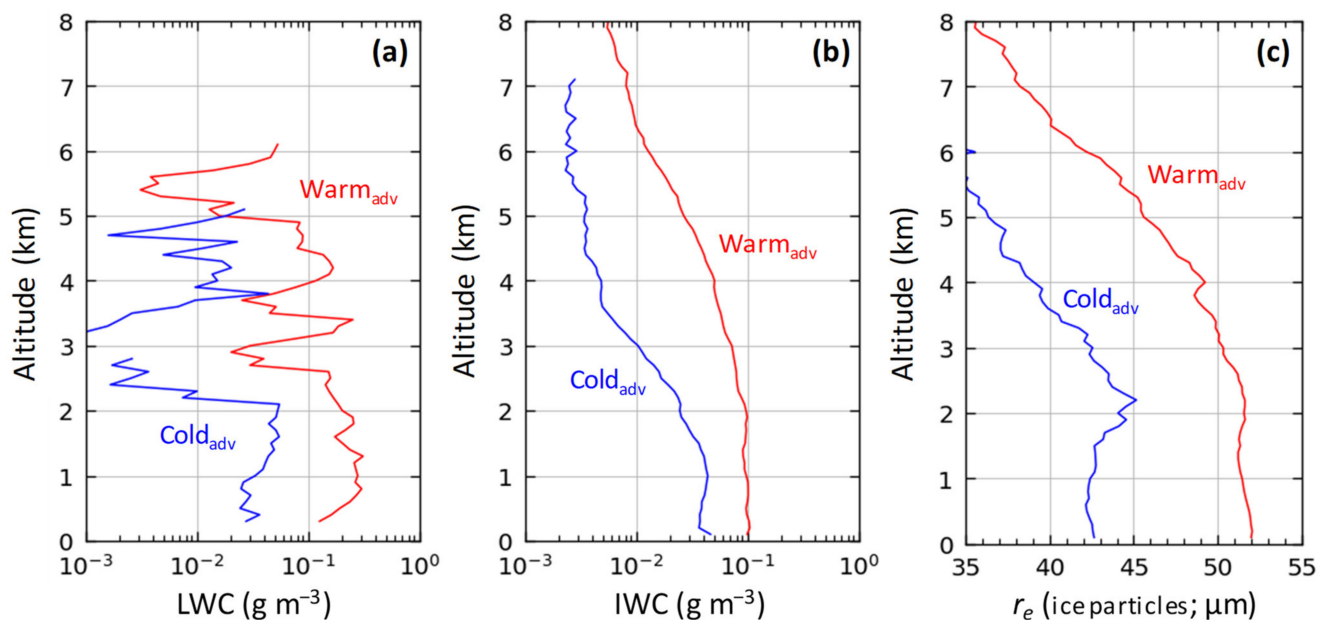


Figure 6. Comparison of the (a) LWC, (b) IWC, and (c) r_e of ice particles between $warm_{adv}$ (red) and $cold_{adv}$ (blue) cases.

3.3. Cloud Longwave Effect: Warm vs. Cold Air Mass Advection

Changes in cloud cover and associated cloud microphysical properties due to alternating warm–moist and cold–dry air masses during winter are directly related to the cloud radiative effects. To further explain the relationships between air mass advection and cloud longwave (LW) effects at Ny-Ålesund, we investigated the frequency distributions of surface LW fluxes during $warm_{adv}$ and $cold_{adv}$ cases (Figure 7). Here, surface-level LW flux data were taken from the Baseline Surface Radiation Network (BSRN) station at

Ny-Ålesund (<https://doi.pangaea.de/10.1594/PANGAEA.914927>; accessed on 26 June 2021) [59], and the LW fluxes under cloud-free conditions were calculated using Santa Barbara Discrete Ordinate Radiative Transfer (DISORT) Atmospheric Radiative Transfer (SBDART) [60]. Mean temperature and relative humidity profiles, which were obtained from radiosonde observations (<https://doi.pangaea.de/10.1594/PANGAEA.914973>; accessed on 26 June 2021) [61] during each advection period, were used as the input for SBDART simulations under the cloud-free condition. Climatological values were used for other input parameters.

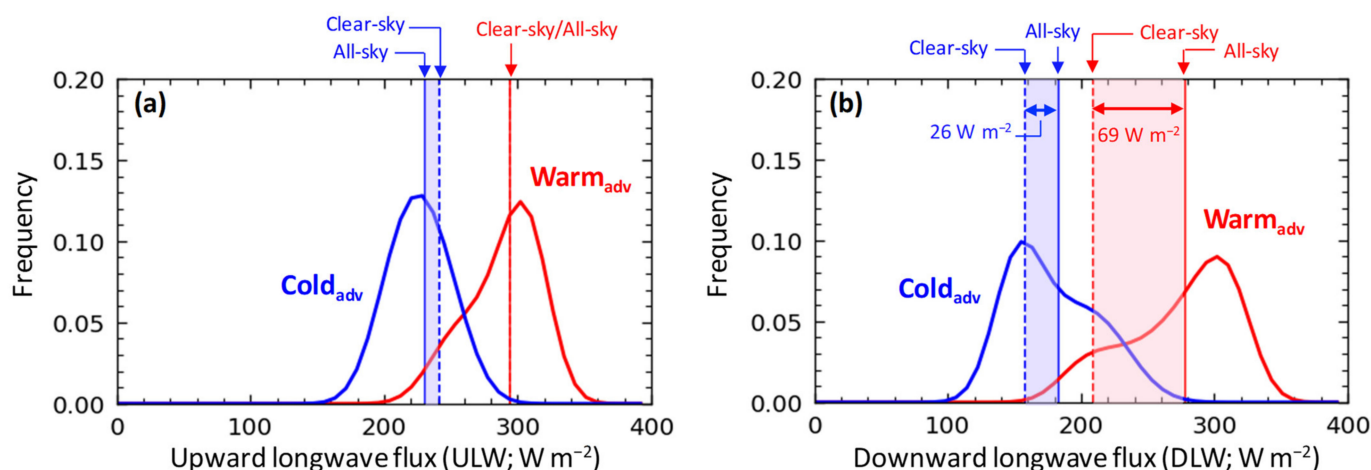


Figure 7. Frequency distributions of (a) ULW fluxes and (b) DLW fluxes under *warm_{adv}* (red) and *cold_{adv}* (blue) cases. Solid vertical line indicates the all-sky LW fluxes from ground-based BSRN radiometer measurements. Dashed vertical line indicates the modeled clear-sky LW fluxes calculated by radiative transfer model (SBDART) simulations using the mean profiles of temperature and humidity from radiosonde measurements. The differences of LW fluxes between all-sky and clear-sky conditions are shown by colored shading. In (b), shaded intervals indicate the increase in DLW fluxes compared to cloud-free conditions under each advection case.

As the upward LW (ULW) fluxes are generally proportional to the surface temperature (i.e., surface emissivity), the average all-sky ULW flux of $293 \pm 24 \text{ W m}^{-2}$ during *warm_{adv}* cases was approximately 30% higher than that for *cold_{adv}* cases ($230 \pm 18 \text{ W m}^{-2}$; Figure 7a). It should be noted that the estimated difference in modeled clear-sky ULW fluxes due to surface temperature bias was less than 10 W m^{-2} . Meanwhile, the average all-sky downward LW (DLW) flux, which depends not only on cloud properties but also on atmospheric water vapor and air temperature, was $278 \pm 39 \text{ W m}^{-2}$ during *warm_{adv}* cases, which was approximately 1.5 times higher than that observed under *cold_{adv}* conditions ($183 \pm 31 \text{ W m}^{-2}$; Figure 7b).

Compared to cloud-free conditions, DLW fluxes increased by 33% (69 W m^{-2}) and 16% (26 W m^{-2}) during the *warm_{adv}* and *cold_{adv}* cases, respectively. In other words, higher CF and cloud water content (LWC and IWC) under *warm_{adv}* periods resulted in elevated downward cloud LW forcing [8,40]. This enhanced downward cloud LW forcing can lead to sea ice melting, thereby increasing upward latent heat fluxes and eventually promoting cloud formation [62–65]. Such triggered feedback mechanisms continue to contribute to surface warming over the Arctic [66,67].

4. Conclusions

This study investigated wintertime cloud properties and radiative effects at Ny-Ålesund, Svalbard, during warm and cold air mass advection periods through a combination of cloud radar, ceilometer, and MWR measurements. The key findings of this study are summarized below.

- The liquid cloud fraction (CF_{liq}) was less than 2%, whereas the ice cloud fraction (CF_{ice}) predominantly exceeded 10% below 6 km during the winter months (November–February). The LWC of mixed-phase clouds (LWC_{mix}), which predominantly exist in the boundary layer (CF_{mix} : 10–30%), was approximately four times higher than that of liquid clouds (LWC_{liq}).
- Eighteen selected cases of warm air mass advection ($warm_{adv}$) were closely linked with strong southerly/southwesterly winds, whereas northerly winds brought cold and dry air masses ($cold_{adv}$) to the study area.
- The total CF of $warm_{adv}$ cases showed a peak around 0.5 km (~60%) due to high CF_{mix} (~30%), and was approximately 20–40% above 2 km altitude. Elevated values of LWC and IWC during $warm_{adv}$ cases can be attributable to the presence of mixed-phase clouds in the boundary layer and ice clouds in the middle troposphere. Consistently, the r_e of ice particles in $warm_{adv}$ cases was approximately 5–10 μm larger than that of $cold_{adv}$ cases at all altitudes.
- Compared to cloud-free conditions, downward longwave (DLW) fluxes increased by 33% (69 W m^{-2}) and 16% (26 W m^{-2}) during $warm_{adv}$ and $cold_{adv}$ cases, respectively.

This study contributes to a better understanding of the relationship between air mass origin and cloud microphysical properties on the Atlantic side of the Arctic. However, future research should conduct a quantitative analysis of how effectively regional-scale or global models simulate the complexity of cloud microphysical properties.

Author Contributions: Conceptualization, S.-W.K.; formal analysis, Y.C., S.-J.P., J.-H.K., H.Y., J.N., S.-Y.J., B.-M.K., and S.-W.K.; writing—original draft preparation, Y.C. and S.-W.K.; writing—review and editing, S.-J.P., J.-H.K., S.-Y.J., B.-M.K., and S.-W.K.; visualization, Y.C.; supervision, S.-W.K. All authors have read and agreed to the published version of the manuscript.

Funding: This research was supported by the Korea Polar Research Institute (PE21010) and R & D Program for Oceans and Polar Regions of the National Research Foundation (NRF) funded by the Ministry of Science and ICT (2020M1A5A1110579).

Data Availability Statement: The ground measurements from cloud radar and ceilometer and retrieved cloud data (e.g., sub-type classification, LWC, and IWC) will be publicly available at the Cloudnet data portal (<https://cloudnet.fmi.fi/>, accessed on 24 May 2021). MWR measurements and additional cloud microphysical properties (e.g., r_e) were obtained from <https://doi.pangaea.de/10.1594/PANGAEA.902183> (accessed on 24 May 2021) [32] and <https://doi.pangaea.de/10.1594/PANGAEA.898556> (accessed on 24 May 2021) [35]. Surface-level LW flux data from BSRN station and radiosonde data can be found at <https://doi.pangaea.de/10.1594/PANGAEA.914927> (accessed on 24 May 2021) [59] and <https://doi.pangaea.de/10.1594/PANGAEA.914973> (accessed on 24 May 2021) [61], respectively. The ERA5 data are accessible at <https://www.ecmwf.int/en/forecasts/datasets/reanalysis-datasets/era5> (accessed on 24 May 2021).

Acknowledgments: The authors appreciate K. Ebell and R. Gierens (University of Cologne) and M. Maturilli (Alfred Wegener Institute for Polar and Marine Research) for their thoughtful and constructive comments. We thank the Cloudnet project office for enabling easy access to the data.

Conflicts of Interest: The authors declare no conflict of interest.

References

1. Curry, J.A.; Schramm, J.L.; Rossow, W.B.; Randall, D. Overview of Arctic cloud and radiation characteristics. *J. Clim.* **1996**, *9*, 1731–1764. [CrossRef]
2. Walsh, J.E.; Chapman, W.L. Arctic cloud–radiation–temperature associations in observational data and atmospheric reanalyses. *J. Clim.* **1998**, *11*, 3030–3045. [CrossRef]
3. Morrison, H.; De Boer, G.; Feingold, G.; Harrington, J.; Shupe, M.D.; Sulia, K. Resilience of persistent Arctic mixed-phase clouds. *Nature Geosci.* **2012**, *5*, 11–17. [CrossRef]
4. Intrieri, J.M.; Fairall, C.W.; Shupe, M.D.; Persson, P.O.G.; Andreas, E.L.; Guest, P.S.; Moritz, R.E. An annual cycle of Arctic surface cloud forcing at SHEBA. *J. Geophys. Res. Oceans* **2002**, *107*, SHE-13. [CrossRef]
5. Kay, J.E.; Gettelman, A. Cloud influence on and response to seasonal Arctic sea ice loss. *J. Geophys. Res. Atmos.* **2009**, *114*, D18204. [CrossRef]

6. Miller, N.B.; Shupe, M.D.; Cox, C.J.; Walden, V.P.; Turner, D.D.; Steffen, K. Cloud radiative forcing at Summit, Greenland. *J. Clim.* **2015**, *28*, 6267–6280. [[CrossRef](#)]
7. Shupe, M.D.; Intrieri, J.M. Cloud radiative forcing of the Arctic surface: The influence of cloud properties, surface albedo, and solar zenith angle. *J. Clim.* **2004**, *17*, 616–628. [[CrossRef](#)]
8. Dong, X.; Xi, B.; Crosby, K.; Long, C.N.; Stone, R.S.; Shupe, M.D. A 10-year climatology of Arctic cloud fraction and radiative forcing at Barrow, Alaska. *J. Geophys. Res. Atmos.* **2010**, *115*, 115. [[CrossRef](#)]
9. Overland, J.E.; Wang, M. Recent extreme Arctic temperatures are due to a split polar vortex. *J. Clim.* **2016**, *29*, 5609–5616. [[CrossRef](#)]
10. Wei, T.; Ding, M.; Wu, B.; Lu, C.; Wang, S. Variations in temperature-related extreme events (1975–2014) in Ny-Ålesund, Svalbard. *Atmos. Sci. Lett.* **2016**, *17*, 102–108. [[CrossRef](#)]
11. Dahlke, S.; Maturilli, M. Contribution of Atmospheric Advection to the Amplified Winter Warming in the Arctic North Atlantic Region. *Adv. Meteorol.* **2017**, *2017*, 1–8. [[CrossRef](#)]
12. Kim, B.M.; Hong, J.Y.; Jun, S.Y.; Zhang, X.; Kwon, H.; Kim, S.J.; Kim, J.H.; Kim, S.W.; Kim, H.K. Major cause of unprecedented Arctic warming in January 2016: Critical role of an Atlantic windstorm. *Sci. Rep.* **2017**, *7*, 40051. [[CrossRef](#)]
13. Maturilli, M.; Kayser, M. Arctic warming, moisture increase and circulation changes observed in the Ny-Ålesund homogenized radiosonde record. *Theor. Appl. Clim.* **2017**, *130*, 1–17. [[CrossRef](#)]
14. Rinke, A.; Maturilli, M.; Graham, R.M.; Matthes, H.; Handorf, D.; Cohen, L.; Hudson, S.R.; Moore, J.C. Extreme cyclone events in the Arctic: Wintertime variability and trends. *Environ. Res. Lett.* **2017**, *12*, 094006. [[CrossRef](#)]
15. Yeo, H.; Park, S.-J.; Kim, B.-M.; Shiobara, M.; Kim, S.-W.; Kwon, H.; Kim, J.-H.; Jeong, J.-H.; Park, S.S.; Choi, T. The observed relationship of cloud to surface longwave radiation and air temperature at Ny-Ålesund, Svalbard. *Tellus B Chem. Phys. Meteorol.* **2018**, *70*, 1–10. [[CrossRef](#)]
16. Yamanouchi, T. Arctic warming by cloud radiation enhanced by moist air intrusion observed at Ny-Ålesund, Svalbard. *Polar Sci.* **2019**, *21*, 110–116. [[CrossRef](#)]
17. Gierens, R.; Kneifel, S.; Shupe, M.D.; Ebell, K.; Maturilli, M.; Löhnert, U. Low-level mixed-phase clouds in a complex Arctic environment. *Atmos. Chem. Phys.* **2020**, *20*, 3459–3481. [[CrossRef](#)]
18. Mioche, G.; Jourdan, O.; Delanoë, J.; Gourbeyre, C.; Febvre, G.; Dupuy, R.; Monier, M.; Szczap, F.; Schwarzenboeck, A.; Gayet, J.-F. Vertical distribution of microphysical properties of Arctic springtime low-level mixed-phase clouds over the Greenland and Norwegian seas. *Atmos. Chem. Phys.* **2017**, *17*, 12845–12869. [[CrossRef](#)]
19. Shupe, M.D.; Walden, V.P.; Eloranta, E.; Uttal, T.; Campbell, J.R.; Starkweather, S.M.; Shiobara, M. Clouds at Arctic atmospheric observatories. Part I: Occurrence and macrophysical properties. *J. Appl. Meteorol. Clim.* **2011**, *50*, 626–644. [[CrossRef](#)]
20. Mioche, G.; Jourdan, O.; Ceccaldi, M.; Delanoë, J. Variability of mixed-phase clouds in the Arctic with a focus on the Svalbard region: A study based on spaceborne active remote sensing. *Atmos. Chem. Phys.* **2015**, *15*, 2445–2461. [[CrossRef](#)]
21. Ebell, K.; Nomokonova, T.; Maturilli, M.; Ritter, C. Radiative effect of clouds at Ny-Ålesund, Svalbard, as inferred from ground-based remote sensing observations. *J. Appl. Meteorol. Clim.* **2020**, *59*, 3–22. [[CrossRef](#)]
22. Nomokonova, T.; Ebell, K.; Löhnert, U.; Maturilli, M.; Ritter, C. The influence of water vapor anomalies on clouds and their radiative effect at Ny-Ålesund. *Atmos. Chem. Phys.* **2020**, *20*, 5157–5173. [[CrossRef](#)]
23. Illingworth, A.J.; Hogan, R.J.; O'Connor, E.J.; Bouniol, D.; Brooks, M.E.; Delanoë, J.; Donovan, D.P.; Eastment, J.D.; Gaussiat, N.; Goddard, J.W.F.; et al. Cloudnet: Continuous evaluation of cloud profiles in seven operational models using ground-based observations. *Bull. Am. Meteorol. Soc.* **2007**, *88*, 883–898. [[CrossRef](#)]
24. Wendisch, M.; Brückner, M.; Burrows, J.; Crewell, S.; Dethloff, K.; Ebell, K.; Lüpkes, C.; Macke, A.; Notholt, J.; Quaas, J. Understanding causes and effects of rapid warming in the Arctic. *Eos* **2017**, *98*. [[CrossRef](#)]
25. Küchler, N.; Kneifel, S.; Löhnert, U.; Kollias, P.; Czekala, H.; Rose, T. A W-Band radar–radiometer system for accurate and continuous monitoring of clouds and precipitation. *J. Atmos. Ocean. Technol.* **2017**, *34*, 2375–2392. [[CrossRef](#)]
26. Maturilli, M.; Ebell, K. Twenty-five years of cloud base height measurements by ceilometer in Ny-Ålesund, Svalbard. *Earth Syst. Sci. Data* **2018**, *10*, 1451–1456. [[CrossRef](#)]
27. Preißler, J.; Martucci, G.; Saponaro, G.; Ovadnevaite, J.; Vaishya, A.; Kolmonen, P.; Ceburnis, D.; Sogacheva, L.; de Leeuw, G.; O'Dowd, C. Six years of surface remote sensing of stratiform warm clouds in marine and continental air over Mace Head, Ireland. *J. Geophys. Res. Atmos.* **2016**, *121*, 14538–14557. [[CrossRef](#)]
28. Intrieri, J.M.; Shupe, M.D.; Uttal, T.; McCarty, B.J. An annual cycle of Arctic cloud characteristics observed by radar and lidar at SHEBA. *J. Geophys. Res. Oceans* **2002**, *107*, SHE-5. [[CrossRef](#)]
29. Crewell, S.; Löhnert, U. Accuracy of cloud liquid water path from ground-based microwave radiometry 2. Sensor accuracy and synergy. *Radio Sci.* **2003**, *38*, 1–7. [[CrossRef](#)]
30. Löhnert, U.; Crewell, S. Accuracy of cloud liquid water path from ground-based microwave radiometry 1. Dependency on cloud model statistics. *Radio Sci.* **2003**, *38*. [[CrossRef](#)]
31. Rose, T.; Crewell, S.; Löhnert, U.; Simmer, C. A network suitable microwave radiometer for operational monitoring of the cloudy atmosphere. *Atmos. Res.* **2005**, *75*, 183–200. [[CrossRef](#)]
32. Nomokonova, T.; Ritter, C.; Ebell, K. *HATPRO Microwave Radiometer Measurements at AWIPEV, Ny-Ålesund (2016–2018)*; PANGAEA: Bremen, Germany, 2019. [[CrossRef](#)]

33. Hogan, R.J.; O'Connor, E.J. Facilitating Cloud Radar and Lidar Algorithms: The Cloudnet Instrument Synergy/Target Categorization Product. Cloudnet Documentation, 2004, 14. Available online: <http://www.met.rdg.ac.uk/clouds/publications/categorization.pdf> (accessed on 26 June 2021).
34. Nomokonova, T.; Ebell, K.; Löhnert, U.; Maturilli, M.; Ritter, C.; O'Connor, E. Statistics on clouds and their relation to thermodynamic conditions at Ny-Ålesund using ground-based sensor synergy. *Atmos. Chem. Phys.* **2019**, *19*, 4105–4126. [\[CrossRef\]](#)
35. Nomokonova, T.; Ebell, K. *Cloud Microphysical Properties Retrieved from Ground-Based Remote Sensing at Ny-Ålesund (10 June 2016–8 October 2018)*; University of Cologne, PANGAEA: Bremen, Germany, 2019. [\[CrossRef\]](#)
36. Hogan, R.J.; Mittermaier, M.P.; Illingworth, A.J. The retrieval of ice water content from radar reflectivity factor and temperature and its use in evaluating a mesoscale model. *J. Appl. Meteorol. Clim.* **2006**, *45*, 301–317. [\[CrossRef\]](#)
37. Frisch, S.; Shupe, M.; Djalalova, I.; Feingold, G.; Poellot, M. The retrieval of stratus cloud droplet effective radius with cloud radars. *J. Atmos. Ocean. Technol.* **2002**, *19*, 835–842. [\[CrossRef\]](#)
38. Miles, N.L.; Verlinde, J.; Clothiaux, E.E. Cloud droplet size distributions in low-level stratiform clouds. *J. Atmos. Sci.* **2000**, *57*, 295–311. [\[CrossRef\]](#)
39. Delanoë, J.; Protat, A.; Bouniol, D.; Heymsfield, A.; Bansemer, A.; Brown, P. The characterization of ice cloud properties from Doppler radar measurements. *J. Appl. Meteorol. Clim.* **2007**, *46*, 1682–1698. [\[CrossRef\]](#)
40. Intrieri, J.M.; Shupe, M.D. Characteristics and radiative effects of diamond dust over the western Arctic Ocean region. *J. Clim.* **2004**, *17*, 2953–2960. [\[CrossRef\]](#)
41. Shupe, M.D. Clouds at Arctic atmospheric observatories. Part II: Thermodynamic phase characteristics. *J. Appl. Meteorol. Clim.* **2011**, *50*, 645–661. [\[CrossRef\]](#)
42. Fukuta, N.; Takahashi, T. The growth of atmospheric ice crystals: A summary of findings in vertical supercooled cloud tunnel studies. *J. Atmos. Sci.* **1999**, *56*, 1963–1979. [\[CrossRef\]](#)
43. Zuidema, P.; Baker, B.; Han, Y.; Intrieri, J.; Key, J.; Lawson, P.; Matrosov, S.; Shupe, M.; Stone, R.; Uttal, T. An Arctic springtime mixed-phase cloudy boundary layer observed during SHEBA. *J. Atmos. Sci.* **2005**, *62*, 160–176. [\[CrossRef\]](#)
44. Verlinde, J.; Harrington, J.Y.; McFarquhar, G.; Yannuzzi, V.; Avramov, A.; Greenberg, S.; Johnson, N.; Zhang, G.; Poellot, M.; Mather, J.H. The mixed-phase Arctic cloud experiment. *Bull. Am. Meteorol. Soc.* **2007**, *88*, 205–222. [\[CrossRef\]](#)
45. Shupe, M.D.; Uttal, T.; Matrosov, S.Y. Arctic cloud microphysics retrievals from surface-based remote sensors at SHEBA. *J. Appl. Meteorol.* **2005**, *44*, 1544–1562. [\[CrossRef\]](#)
46. Wegener, A. *Thermodynamik der Atmosphäre*; J.A. Barth: Leipzig, Germany, 1911.
47. Bergeron, T. On the physics of clouds and precipitation. In *Procès-Verbaux de l'Association de Météorologie*; International Union of Geodesy and Geophysics: Potsdam, Germany, 1935; pp. 156–178.
48. Findeisen, W. Kolloid-meteorologische Vorgänge bei Neiderschlags-bildung. *Meteorol. Z.* **1938**, *55*, 121–133.
49. Curry, J.; Herman, G. Relationships between large-scale heat and moisture budgets and the occurrence of Arctic stratus clouds. *Mon. Weather Rev.* **1985**, *113*, 1441–1457. [\[CrossRef\]](#)
50. Johansson, E.; Devasthale, A.; Tjernström, M.; Ekman, A.M.; L'Ecuyer, T. Response of the lower troposphere to moisture intrusions into the Arctic. *Geophys. Res. Lett.* **2017**, *44*, 2527–2536. [\[CrossRef\]](#)
51. Serreze, M.C.; Barrett, A.P.; Cassano, J.J. Circulation and surface controls on the lower tropospheric air temperature field of the Arctic. *J. Geophys. Res. Atmos.* **2011**, *116*. [\[CrossRef\]](#)
52. Eldevik, T.; Risebrobakken, B.; Bjune, A.E.; Andersson, C.; Birks, H.J.B.; Dokken, T.M.; Drange, H.; Glessmer, M.S.; Li, C.; Nilsen, J.E.Ø. A brief history of climate—the northern seas from the Last Glacial Maximum to global warming. *Quat. Sci. Rev.* **2014**, *106*, 225–246. [\[CrossRef\]](#)
53. Shupe, M.D.; Matrosov, S.Y.; Uttal, T. Arctic mixed-phase cloud properties derived from surface-based sensors at SHEBA. *J. Atmos. Sci.* **2006**, *63*, 697–711. [\[CrossRef\]](#)
54. De Boer, G.; Eloranta, E.W.; Shupe, M.D. Arctic mixed-phase stratiform cloud properties from multiple years of surface-based measurements at two high-latitude locations. *J. Atmos. Sci.* **2009**, *66*, 2874–2887. [\[CrossRef\]](#)
55. Mewes, D.; Jacobi, C. Heat transport pathways into the Arctic and their connections to surface air temperatures. *Atmos. Chem. Phys.* **2019**, *19*, 3927–3937. [\[CrossRef\]](#)
56. Liu, Y.; Key, J.R.; Vavrus, S.; Woods, C. Time evolution of the cloud response to moisture intrusions into the Arctic during winter. *J. Clim.* **2018**, *31*, 9389–9405. [\[CrossRef\]](#)
57. Hobbs, P.V.; Rangno, A.L. Ice particle concentrations in clouds. *J. Atmos. Sci.* **1985**, *42*, 2523–2549. [\[CrossRef\]](#)
58. Hobbs, P.V.; Rangno, A.L. Microstructures of low and middle-level clouds over the Beaufort Sea. *Q. J. R. Meteorol. Soc.* **1998**, *124*, 2035–2071. [\[CrossRef\]](#)
59. Maturilli, M. *Basic and Other Measurements of Radiation at Station Ny-Ålesund (2006-05 Et Seq)*; Alfred Wegener Institute—Research Unit Potsdam, PANGAEA: Bremen, Germany, 2020. [\[CrossRef\]](#)
60. Ricchiazzi, P.; Yang, S.; Gautier, C.; Sowle, D. SBDART: A research and teaching software tool for plane-parallel radiative transfer in the Earth's atmosphere. *Bull. Am. Meteorol. Soc.* **1998**, *79*, 2101–2114. [\[CrossRef\]](#)
61. Maturilli, M. *High Resolution Radiosonde Measurements from Station Ny-Ålesund (2017-04 Et Seq)*; Alfred Wegener Institute—Research Unit Potsdam, PANGAEA: Bremen, Germany, 2020. [\[CrossRef\]](#)
62. Liu, Y.; Key, J.R.; Liu, Z.; Wang, X.; Vavrus, S.J. Cloudier Arctic expected with diminishing sea ice. *Geophys. Res. Lett.* **2012**, *39*. [\[CrossRef\]](#)

-
63. Park, D.-S.R.; Lee, S.; Feldstein, S.B. Attribution of the Recent Winter Sea Ice Decline over the Atlantic Sector of the Arctic Ocean. *J. Clim.* **2015**, *28*, 4027–4033. [[CrossRef](#)]
 64. Jun, S.-Y.; Ho, C.-H.; Jeong, J.-H.; Choi, Y.-S.; Kim, B.-M. Recent changes in winter Arctic clouds and their relationships with sea ice and atmospheric conditions. *Tellus A Dyn. Meteorol. Oceanogr.* **2016**, *68*, 68. [[CrossRef](#)]
 65. Woods, C.; Caballero, R. The role of moist intrusions in winter Arctic warming and sea ice decline. *J. Clim.* **2016**, *29*, 4473–4485. [[CrossRef](#)]
 66. Francis, J.A.; Hunter, E. New insight into the disappearing Arctic sea ice. *Eos Trans. Am. Geophys. Union* **2006**, *87*, 509–511. [[CrossRef](#)]
 67. Screen, J.A.; Simmonds, I. The central role of diminishing sea ice in recent Arctic temperature amplification. *Nature* **2010**, *464*, 1334–1337. [[CrossRef](#)] [[PubMed](#)]